Coupled Systems Mechanics, Vol. 1, No. 4 (2012) 361-379
DOI: http://dx.doi.org/10.12989/csm.2012.1.4.361

Combined multi-predict-correct iterative method for interaction between pulsatile flow and large deformation structure

Wenquan Wang*[1], Zhang Li-xiang[1], Yan Yan[1] and Yakun Guo[2]

[1]*Department of Engineering Mechanics, Kunming University of Science and Technology, Kunming 650051, China*
[2]*School of Engineering, University of Aberdeen, Aberdeen AB24 3UE, UK*

(Received July 27, 2012, Revised November 21, 2012, Accepted November 27, 2012)

Abstract. This paper presents a fully coupled three-dimensional solver for the analysis of interaction between pulsatile flow and large deformation structure. A partitioned time marching algorithm is employed for the solution of the time dependent coupled discretised problem, enabling the use of highly developed, robust and well-tested solvers for each field. Conservative transfer of information at the fluid-structure interface is combined with an effective multi-predict-correct iterative scheme to enable implicit coupling of the interacting fields at each time increment. The three-dimensional unsteady incompressible fluid is solved using a powerful implicit time stepping technique and an ALE formulation for moving boundaries with second-order time accurate is used. A full spectrum of total variational diminishing (TVD) schemes in unstructured grids is allowed implementation for the advection terms and finite element shape functions are used to evaluate the solution and its variation within mesh elements. A finite element dynamic analysis of the highly deformable structure is carried out with a numerical strategy combining the implicit Newmark time integration algorithm with a Newton-Raphson second-order optimisation method. The proposed model is used to predict the wave flow fields of a particular flow-induced vibrational phenomenon, and comparison of the numerical results with available experimental data validates the methodology and assesses its accuracy. Another test case about three-dimensional biomedical model with pulsatile inflow is presented to benchmark the algorithm and to demonstrate the potential applications of this method.

Keywords: fluid-structure interaction; pulsatile flow; partitioned analysis; multi-predict-correct iterative; arbitrary lagrangian-eulerian; experimental test

1. Introduction

The engineering modeling of multi-physics and multi-field phenomena has over the past few decades stimulated enormous interest among scientists. In recent years, fluid-structure interaction (FSI) problems in particular have received increasing attention from the computational mechanics community. This has been made possible by the advances in the computational modeling of both fluid and solid structures and further galvanized by significant developments in terms of affordable computational resources. The application of numerical methods to the solution of a coupled field

* Corresponding author, Dr., E-mail: wwqquan@126.com

problem results in a system of nonlinear algebraic equations which may be resolved according to either a monolithic (Sarrate *et al*. 2001, Rugonyi and Bathe 2001, Heil 2004) or a partitioned approach (Wang *et al*. 2009, Zhang *et al*. 2007, Stein *et al*. 2001). A monolithic solution strategy treats all the domains simultaneously and the fluid and the structural equations are tightly coupled and solved together, leading to a single set of algebraic equations involving all the relevant variables. Such schemes are advantageous in that the kinetic boundary conditions at the interface are solved simultaneously within the fluid and the structure domains, resulting in a stable scheme with rapid convergence and less restriction on the permissible time step. However, it is generally considered too numerically inefficient or even impossible to solve both the fluid and structure system equations using a single numerical scheme (Heil 2004, Liew *et al*. 2007), with the monolithic schemes developed so far demonstrating simple, academic problems (Guruswamy and Byun 1994, Blom 1998, Hübner 2004). In contrast, if a partitioned approach is adopted then each physical field is separately defined, discretised and numerically solved, with coupling procedures applied to transfer the required interface information. Although the interacting fields are not solved simultaneously, a partitioned coupling scheme can require very few resolutions of the coupled problem at each time step for sufficient coupling to be achieved. These schemes are found to be very attractive as they allow the modularity of each of the field solvers to be retained (Bletzinger *et al*. 2006), enabling the use of highly developed specialised codes that can be tailored to the specific problem at hand. Two contrasting approaches towards the definition of the multi-field problem can also be identified, namely fixed mesh (Zhang and Zheng 2007, Ge and Sotiropoulos 2007, Lee *et al*. 2008, Hieber and Koumoutsakos 2008) and dynamics mesh (Donea 1983, Ramaswamy and Kawahara 1987, Farhat *et al*. 2000). The former encompasses a range of closely-related methods which originate from the immersed boundary method, pioneered by Peskin *et al*.(1972), whilst within the latter category, one of the most well-known techniques is the arbitrary Lagrangian-Eulerian (ALE) formulation (Hughes *et al*. 1981, Donea *et al*. 1982). Although immersed techniques are commonly used for problems involving large deformations or fragmentation, one key feature of a dynamic mesh approach which is particularly advantageous is the ability to capture very accurately the position of the moving fluid-structure interface. This work adopts a partitioned, boundary-fitted ALE approach whereby the solid structure, along with natural boundary conditions provided by the Cauchy stress field generated at the fluid-structure interface, is analysed in a standard finite element manner and resolved using a Lagrangian description in order to accurately model the large deformation or large strain structure. Within the fluid domain, the ALE Navier-Stokes equations are resolved for the deforming fluid domain along with kinematic boundary conditions which ensure compatibility at the interface as well as geometric conservation on the deforming fluid domain.

Within current FSI research, time-dependent problems, especially for the pulsatile or wave flow involving large structural deformations are of particular interest with potential applications ranging from lightweight structural membranes to complex biomedical modeling (Bungartz *et al*. 2006, Torii *et al*. 2008, Tezduyar *et al*. 2006). The FSI problem are some additional characters. Firstly, the fluid solver must be deal with the advection-dominated flows and the unsteady inertial force well, which is suggested that it must be very carefully to select the discrete scheme of advection term and time term, especially for the simulation of advection-dominated flows on the unstructured grid, otherwise, the fluid solver is very difficult to convergence. Secondly, large structural deformations or nonlinear material characters are often considered. Thirdly, the synchronously advance of time discretization between the fluid and solid solvers is very necessary to avoid the error due to the time lag of fluid or solid solver. Finally, some experimental data are lack for verifying the numerical method. Of

course, the common issues for FSI, such as the mesh movement method, the geometry conserve law (GCL) and information transfer on the interfaces between the fluid and solid, etc, are also important in implementing FSI calculation.

In order to resolve the above interaction problem, some strategies are adopted. Firstly, the three-dimensional unsteady incompressible fluid is solved using a powerful implicit time stepping technique and an ALE formulation for moving boundaries with second-order time accurate is used. Secondly, a full spectrum of total variational diminishing (TVD) schemes in unstructured grids is allowed implementation for the advection terms and finite element shape functions are used to evaluate the solution and its variation within mesh elements. Thirdly, a finite element dynamic analysis of the highly deformable structure is carried out with a numerical strategy combining the implicit Newmark time integration algorithm with a Newton-Raphson second-order optimisation method. Lastly, a robust and efficient multi-predict-correct iterative scheme to enable implicit coupling of the interacting fields at each time increment. Finally, some experimental data are gained for verifying the validity of the numerical method, which is also a formidable work.

2. Unsteady fluid flow with moving boundaries

2.1 Governing equations

The ALE method is utilized to describe deformable fluid domains. The ALE formulation of the control equations for an viscous Newtonian fluid can be expressed as

$$\rho^f\left(\frac{\partial u_i^f}{\partial t}\right)+\rho^f(u_j^f-u_j^{ale})\frac{\partial u_i^f}{\partial u_j}=-\frac{\partial p}{\partial x_i}+\frac{\partial}{\partial x_j}\left[\mu^f\left(\frac{\partial u_i^f}{\partial x_j}+\frac{\partial u_j^f}{\partial x_i}\right)\right]+f_i \tag{1}$$

$$\frac{\partial u_j^f}{\partial x_j}=0 \tag{2}$$

Where ρ^f is the mass density of the fluid, u_i^f is the ith component of the fluid velocity vector, u_j^{ale} is the jth component of the grid velocity vector, p is the pressure of the fluid, f_i is the ith component of body force and μ^f is the dynamic viscosity of the fluid.

2.2 Treatment of the ALE fluxes

An important property of Eq. (1) is geometric conservation. The GCL (Thomas and Lombard 1979), requires that the control volume movement itself has no direct effect on the fluxes, in the sense that if the unknown field is constant, the numerical solution does not change in time in the presence of a moving mesh, i.e., with respect to dynamic meshes, the integral form of the conservation Eq. (1) for a general scalar ϕ, on an arbitrary control volume, V, whose boundary is moving can be written as

$$\frac{d}{dt}\int_V\rho^f\phi dV+\int_{\partial V}\rho^f\phi(\boldsymbol{u}-\boldsymbol{u}^{ale})\cdot dA=\int_{\partial V}\Gamma\nabla\phi\cdot dA+\int_V S_\phi dV \tag{3}$$

where $\boldsymbol{u}$ is the flow velocity vector, $\boldsymbol{u}^{ale}$ is the grid velocity of the moving mesh, Γ is the diffusion coefficient, S_ϕ is the source term of ϕ and ∂V is used to represent the boundary of the control

volume V. It is desirable to retain this quality numerically after discretisation. This has led to the so-called discrete geometric conservation law (DGCL), as advocated by Lesoinne *et al*. (1996), Koobus and Farhat (1999), Farhat *et al*. (2001), Nkonga and Guillard (1994), Venkatakrishnan and Mavriplis (1996), which governs the geometric parameters of the numerical scheme, such as grid positions and velocities, so that the corresponding numerical scheme reproduces exactly a constant solution.

The time derivative term in Eq. (3) can be written, using a second-order backward difference scheme, as

$$\frac{d}{dt}\int_V \rho^f \phi dV = \frac{\frac{3}{2}(\rho^f \phi V)^{n+1} - 2(\rho^f \phi V)^n + \frac{1}{2}(\rho^f \phi V)^{n-1}}{\Delta t} \tag{4}$$

Where n denote the respective quantity at a time level t^n.

In order to satisfy the GCL, The $(n+1)$ th time level the time-averaging computational volume $\overline{V}^{n+1}$ of the convective fluxes, diffusive and source terms is computed from

$$\overline{V}^{n+1} = \frac{1}{2}V^{n+1} + V^n - \frac{1}{2}V^{n-1} \tag{5}$$

and the ALE term is expressed as

$$\int_{\partial V} \boldsymbol{u}^{ale} \cdot dA = \sum_j^{n_f} u_j^{ale} \cdot A_j \tag{6}$$

where n_f is the number of faces on the control volume and A_j is the j face area vector. The dot product $u_j^{ale} \cdot A_j$ on each control volume face is calculated from

$$u_j^{ale} \cdot A_j = \frac{\frac{3}{2}\delta V_j^{n+1} - \frac{1}{2}\delta V_j^n}{\Delta t} \tag{7}$$

Where δV_j^n, δV_j^{n+1} are the volume swept out by the control volume face j over the nth time step $t^n - t^{n-1}$ and $(n+1)$ th time step $t^{n+1} - t^n$, respectively. The ALE version of the three-point backward difference scheme in Eq. (4) combined Eqs. (5)-(7) is second-order time-accurate on moving grids, which is proofed by Geuzaine *et al.* (2003).

For the moving mesh of fluid region, we simply make the fluid mesh displacements satisfy a harmonic extension of the moving fluid-structure boundary.

2.3 Treatment the advection term

Following Roe (1983), the finite volume element surface value φ_f of a TVD scheme is written as the sum of a diffusive first order upwind term and an anti-diffusive one. The anti-diffusive part is multiplied by the flux limiter function, $\psi(r)$, which is a non-linear function of r. As shown in Fig. 1, nodes C and D are defined as the upwind and downwind nodes around face f_i (where the value of an integration point ϕ_{pi} is approximately equal to φ_{fi}), and the virtual U node is defined as the node upwind of the C node. The surface value φ_{fi} of face f_i can be written as

$$\varphi_{fi} = \varphi_{pi} = \varphi_C + \frac{1}{2}\psi(r_f)(\varphi_D - \varphi_C) \tag{8}$$

and the r ratio becomes

$$r_{fi} = \frac{\varphi_C - \varphi_U}{\varphi_D - \varphi_C} = \frac{\varphi_D + (\varphi_C - \varphi_U) - \varphi_D}{\varphi_D - \varphi_C} = \frac{(\varphi_D - \varphi_U) - (\varphi_D - \varphi_C)}{\varphi_D - \varphi_C} \tag{9}$$

Noting that values for φ_D and φ_C represent the values of the nodes straddling the interface and thus are readily available for unstructured grid. Therefore, the r-values would be computable if the term involving φ_U could be replaced by a known term. In this case

$$(\varphi_D - \varphi_U) = \nabla\varphi_C \cdot \boldsymbol{r}_{UD} = 2\nabla\varphi_C \cdot \boldsymbol{r}_{CD} \approx 4\nabla\varphi_C \cdot \boldsymbol{r}_{CP_i} \tag{10}$$

where $\boldsymbol{r}_{CD}$ is the vector between the nodes C and D, and $\boldsymbol{r}_{CP_i}$ is the vector between nodes C and the virtual node P_i and $\boldsymbol{r}_{UD}$ is the vector between nodes D and the virtual node U, representing the node upstream of node C (see Fig. 1). Node U is chosen such that it lies along the line joining nodes D and C with C at the center of the 'UD' segment. Other positions of U could also be chosen, but with a loss of accuracy as the nodal gradient yields a second order accuracy only when the difference is centered at node C.

The formulation of r becomes

$$r_f = \frac{4\nabla\varphi_C \cdot \boldsymbol{r}_{CPi} - (\varphi_D - \varphi_C)}{\varphi_D - \varphi_C} = \frac{4\nabla\varphi_C \cdot \boldsymbol{r}_{CPi}}{\varphi_D - \varphi_C} - 1 \tag{11}$$

which can be easily computed for unstructured grids. Where MUSCL (monotonic upstream-centered scheme for conservation laws) limiter $\psi(r_f) = (r_f + |r_f|)/(1 + |r_f|)$ is used.

Volumetric terms are converted into their discrete form by approximating specific values in each sector and then integrating those values over all sectors that contribute to a control volume. Surface flow terms are converted into their discrete form by first approximating fluxes at integration points, P_i, which are located at the center of each surface segment in a 3D element surrounding the control volume. Flows are then evaluated by integrating the fluxes over the surface segments that contribute to a control volume.

$$\int_{\partial V(t)} \rho^f u_j^f u_i^f n_j dS = \sum_{p_i} (\rho^f u_j^f n_j \Delta S_j)_{p_i} (u_i^f)_{p_i} \tag{12}$$

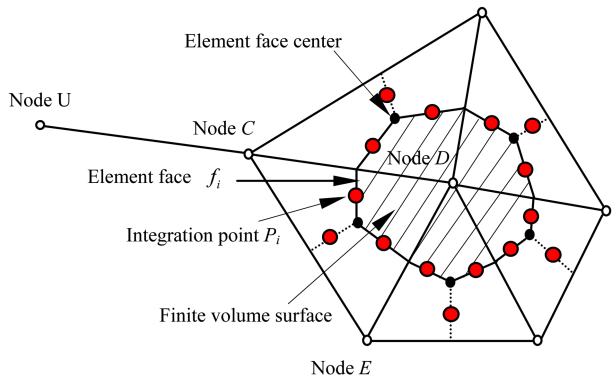

Fig. 1 mesh element and control volume surface

Where the subscript P_i denotes evaluation at an integration point, and summations are over all the integration points of the control volume.

2.4 Treatment the diffusion term

The solution fields are stored at the mesh nodes. However, various terms in the equations require solutions or solution gradients to be approximated at integration points. Finite element shape functions are consequently used to evaluate the solution and its variation within mesh elements.

A variable ϕ varies within an element as follows

$$\phi = \sum_{i=1}^{N_{node}} N_i \phi_i \tag{13}$$

where N_i is the shape function for node i and ϕ_i is the value of ϕ at node i. The summation is over all nodes of an element. Following the standard finite element approach, shape functions are used to evaluate spatial derivatives for all the diffusion terms. For example, for a derivative in the x direction at integration point P_i

$$\left.\frac{\partial \phi}{\partial x}\right|_{P_i} = \sum_n \left.\frac{\partial N_n}{\partial x}\right|_{P_i} \phi_n \tag{14}$$

The summation is over all the shape functions for the element. The Cartesian derivatives of the shape functions can be expressed in terms of their local derivatives via the Jacobian transformation matrix

$$\begin{bmatrix} \frac{\partial N}{\partial x} \\ \frac{\partial N}{\partial y} \\ \frac{\partial N}{\partial z} \end{bmatrix} = \begin{bmatrix} \frac{\partial x}{\partial \xi} & \frac{\partial y}{\partial \xi} & \frac{\partial z}{\partial \xi} \\ \frac{\partial x}{\partial \zeta} & \frac{\partial y}{\partial \zeta} & \frac{\partial z}{\partial \zeta} \\ \frac{\partial x}{\partial \eta} & \frac{\partial y}{\partial \eta} & \frac{\partial z}{\partial \eta} \end{bmatrix} \tag{15}$$

The shape function gradients can be evaluated at the actual location of each integration point, or at the location where each P_i surface intersects the element edge (i.e., linear-linear interpolation). The latter formulation improves solution robustness at the expense of locally reducing the spatial order-accuracy of the discrete approximation.

The discrete form of the diffusion term of integral equations becomes

$$\int_{\partial V(t)} \left[\mu^f \left(\frac{\partial u_i^f}{\partial x_j} + \frac{\partial u_j^f}{\partial x_i} \right) \right] n_j dS = \sum_{p_i} \left[\mu^f \left(\frac{\partial u_i^f}{\partial x_j} + \frac{\partial u_j^f}{\partial x_i} \right) n_j \Delta S \right]_{p_i} \tag{16}$$

2.5 Physical time discretisation

The three level, second order, backward difference representation for a control volume

$$\frac{d}{dt} \int_{V_I(t)} \rho^f u_i^f dV = \frac{1}{\Delta t} \left(\frac{3}{2} V_I^{n+1} \rho^{n+1,f} u_i^{n+1,f} - 2 V_I^n \rho^{n,f} u_i^{n,f} + \frac{1}{2} V_I^{n-1} \rho^{n-1,f} u_i^{n-1,f} \right) \tag{17}$$

is employed for the approximation of the physical time derivative, where the superscript n denotes an evaluation at time $t = t^n$, where $\Delta t = t^{n+1} - t^n$ denotes the physical time step.

3. Finite element model for structure dynamics

3.1 Governing equations

Let Ω_t^s be the spatial domain of a structure with the boundary ∂R_t^s, which is composed of mechanical and geometrical boundary conditions, at time t. Here, the superscript s stands for the structural component. The equilibrium equation for the structure is

$$\rho^s \frac{d^2 u_i^s}{dt^2} = \frac{\partial \sigma_{ji}^s}{\partial x_j} + \rho^s g_i^s \text{ in } \Omega_t^s \tag{18}$$

where ρ^s is the mass density of the structure, u_i^s is the ith component of the structural displacement vector, σ_{ji}^s is the ijth component of the stress tensor of the structure, and g_i^s the body force vector acting on the structure. Strain is assumed to be small, hence a materially linear elastic model is used.

3.2 Finite element discretisation and solution

The solution of the virtual work representation of the dynamic equilibrium equations given in Eq. (18) is found at discrete time intervals for given material and loading conditions by determining a deformed configuration, that is in a state of dynamic equilibrium. When the geometric nonlinear is consieded, the dynamic equilibrium equations can be written as

$$[M]\{\ddot{u}\} + [C]\{\dot{u}\} + \{\Phi\} = \{P\} \tag{19}$$

Where $[M]$ is the mass matrix, $[C]$ is the dampness matrix. $\{\Phi\} = \int [\bar{B}]^T \{u\} dV$ is nonlinear term, where

$$[\bar{B}] = [B_0] + [B_L] \tag{20}$$

Where $[B_0]$ is the linear strain term independent on $\{\delta\}$, $[B_L]$ is the nonlinear strain term dependent on $\{u\}$, and $\{\sigma\}$ is the stress, which is written as

$$\{\sigma\} = [D](\{\varepsilon\} - \{\varepsilon_0\}) + \{\sigma_0\} \tag{21}$$

Where $[D]$ is the elastic matrix, $\{\varepsilon_0\}$ is the initial strain, $\{\sigma_0\}$ is the initial stress.

This equilibrium configuration is found by means of a Newmark time integration scheme in conjunction with a Newton-Raphson iterative solution procedure, and therefore, requires a linearised form of the nonlinear dynamic equilibrium equations. Taking

$$\{\Phi\}_{t+\Delta t} = \{\Phi\}_t + [K_T]_t \Delta\{u\} \tag{22}$$

Where $[K_T]_t$ is the tangent stiffness matrix at time t, which is gained by the displacement $\{u\}_t$ at time

t. Substitute Eq. (22) into Eq. (19), the linearized dynamic equilibrium equation can be expressed as

$$[M]\{\ddot{u}\}_{t+\Delta t} + [C]\{\dot{u}\}_{t+\Delta t} + [K_T]_t \Delta\{u\} = \{P\}_{t+\Delta t} - \{\Phi\}_t \tag{23}$$

Considering the implicit Newmark time integration scheme, the algorithm relating the approximations to the displacement, velocity and acceleration at time t, denoted $\{u\}$, $\{\dot{u}\}$ and $\{\ddot{u}\}$, respectively, can be stated in its general form as

$$\{\ddot{u}\}_{t+\Delta t} = \frac{1}{\beta \Delta t^2}(\{u\}_{t+\Delta t} - \{u\}_t) - \frac{1}{\beta \Delta t}\{\dot{u}\}_t - \left(\frac{1}{2\beta} - 1\right)\{\ddot{u}\}_t \tag{24}$$

$$\{\dot{u}\}_{t+\Delta t} = \frac{\gamma}{\beta \Delta t}(\{u\}_{t+\Delta t} - \{u\}_t) - \left(\frac{\gamma}{\beta} - 1\right)\{\dot{u}\}_t - \frac{\Delta t}{2}\left(\frac{\gamma}{\beta} - 2\right)\{\ddot{u}\}_t \tag{25}$$

where β and γ are non-dimensional parameter, $\beta \in [0,1]$, $\gamma \in [0,1]$. Substitute Eqs. (24) and (25) into Eq. (23), gain

$$[\hat{K}]\{u\}_{t+\Delta t} = \{\hat{R}\}_{t+\Delta t} \tag{26}$$

Where $\hat{K}$ is the effective stiffness matrix, which can be expressed as

$$[\hat{K}] = \frac{1}{\beta \Delta t^2}[M] + \frac{\gamma}{\beta \Delta t}[C] + [K_T] \tag{27}$$

$\{\hat{R}\}_{t+\Delta t}$ is the effective loading matrix, can be expressed as

$$\begin{aligned}\{\hat{R}\}_{t+\Delta t} = \{P\}_{t+\Delta t} - \{\Phi\}_f + [M]\left(\frac{1}{\beta \Delta t^2}\{u\}_t + \frac{1}{\beta \Delta t}\{\dot{u}\}_t + \left(\frac{1}{2\beta} - 1\right)\{\ddot{u}\}_t\right) \\ + [C]\left(\frac{\gamma}{\beta \Delta t}\{u\}_t + \left(\frac{\gamma}{\beta} - 1\right)\{\dot{u}\}_t + \frac{\Delta t}{2}\left(\frac{\gamma}{\beta} - 2\right)\{\ddot{u}\}_t\right)\end{aligned} \tag{28}$$

A Newton-Raphson iterative solution procedure is used to solve the nonlinear Eq. (26), namely

$$\{\Delta u\}_n = -[\hat{K}]^{-1}\{\hat{R}\}_n \tag{29}$$

$$\Delta\{u\} = \{u\}_{t+\Delta t} - \{u\}_t \tag{30}$$

4. Combined multi-predict-correct iterative coupling method

The well known and commonly used conventional serial staggered solution algorithm of Farhat and Lesoinne (2000), where the solution is advanced in time after a single pass through the individual field solvers and exchange of data, is capable of applying a loose coupling between interacting fields. However, by building an iterative procedure into the method at each time step, the whole process can then systematically correct the initial values for the variables until convergence is reached. Following Farhat and Lesoinne (2000), a staggered solution procedure with full convergence subiteration at each time step is proposed to ensure strong coupling of the partitioned fluid

and structure fields. If one subsystem - say the fluid - is solved first so that with these newly computed values the second subsystem - the structure - is also solved, then the scheme corresponds to a predict/correct method, shown in Fig. 2. When implemented in conjunction with the implicit time stepping scheme of the fluid solver and the implicit Newmark/Newton-Raphson scheme of the structural solver. This subiterative approach is particularly attractive as it enables a large physical time step to be applied without impairing the long term stability of the coupled solution. Depending on the size of the time step selected, subiterations may or may not be required at each time step for the convergence of the coupled solution.

The proposed iterative scheme can be outlined as follows:

(1) Use known structural displacements and velocity at t^{n-1} to predict/correct the motion of the structure at t^n, namely, predicted velocity $\tilde{\dot{u}}_n^s = \dot{u}_{n-1}^s + \alpha\Delta t\ddot{u}_{n-1}^s$ and displacement $\tilde{u}_n^s = u_{n-1}^s + \alpha\Delta t\dot{u}_{n-1}^s$, where α is a non-dimensional parameter, $\alpha \in [0,1]$.

(2) Transfer the predicted velocity and displacement of structure to the fluid and dynamic mesh systems, $\tilde{\dot{x}}_n^f = \tilde{\dot{u}}_n^s$, $\tilde{x}_{n+1/2}^f = \tilde{x}_{n-1/2}^f + \Delta t\dot{x}_n^f$ and generate the updated fluid domain mesh and corresponding fluid domain mesh velocities.

(3) Compute the new fluid domain unknowns, namely fluid pressure $\tilde{p}_{n+1/2}^f$ and velocity fields $\tilde{u}_{n+1/2}^f$, which satisfy the displacement and velocity boundary conditions of the moving fluid-structure interface.

(4) Transfer the new fluid pressure field $\tilde{p}_{n+1/2}^f$ to the structural discretisation and calculate the updated structural loading.

(5) Compute the new dynamic structure domain unknowns at t^n, namely acceleration $\ddot{u}_n^s$, velocity $\dot{u}_n^s$ and displacement u_n^s in response to the fluid loading.

(6) Compare u_n^s with $\tilde{u}_n^s$ if $\|u_n^s - \tilde{u}_n^s\| / \|u_n^s\| \le \varepsilon$ is satisfied, where ε is the iteration control parameter, enter into calculation of next time step, if not, take the u_n^s and $\dot{u}_n^s$ as new predicting value $\tilde{u}_n^s$ and $\tilde{\dot{u}}_n^s$, loop step (2) to step (5), until stratified precision requirement .

Dirichlet boundary conditions, extracted from structural displacements u_n^s, prescribe the position of the fluid-structure interface and are enforced by the dynamic mesh algorithm when generating the updated fluid domain discretisation. This work adopts the converged position of the interface from the preceding time step an initial prediction, and thereafter applies the interface position of the moving structure at the current subiteration. However, techniques such as damping, under-relaxation or more sophisticated forms of preconditioning could readily be applied to improve convergence by modifying the predicted/corrected terms within the subiterative scheme. The ALE mesh velocities in the fluid domain u_n^{ale} are calculated from the mesh displacements according to the second-order

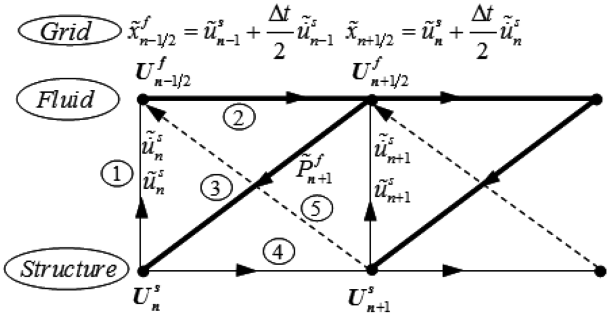

Fig. 2 Simultaneously iterate procedure

backwards difference scheme in order to maintain consistency with the discrete time integration scheme of the fluid solver.

For strong coupling of the interacting fields it is imperative that both displacement and velocity boundary conditions are satisfied at the fluid-structure interface before the solution is advanced in time. The partitioned solution scheme employed here ensures that the compatibility of the fluid and structural domain displacement fields is maintained at the interface at every subiteration, by consistently applying the structural displacements at the interface as Dirichlet boundary conditions for the dynamic mesh algorithm. Compatibility of the fluid and structure velocity fields at the interface is achieved as a result of the predict/corrective subiterations method.

5. Numerical examples

5.1 Flow-induced vibration of a flexible beam

5.1.1 Computational setup

A fixed cubic rigid body of side $D = 100$ mm is centrally placed in an incompressible fluid (water) and secured on between the up and bottom walls to eliminate the possibility of vibrations. A flexible thin elastic plate with a 300 mm long, 98 mm wide and 4 mm thick is attached to the rigid body in the centre of the downstream face. The material parameters of the plate is taken as, respectively, the density $\rho_s = 1280$ kg/m^3, the Young's modulus $E_s = 2.6 \times 10^9$ Pa and the Poisson's ratio $\nu = 0.35$. The undamped natural frequency of the first bending mode of the plate $f_1 = 14$ Hz, and the second bending mode of the plate $f_2 = 62$ Hz. The vortices, which separate from the corners of the rigid body upstream, generate lift forces which excite oscillations of the elastic plate downstream. The flow Reynold number is defined as $Re = VD/\upsilon$, where V is average inflow velocity of the test section, υ is kinematic viscosity of the water at 291 K. Control points of structure are $A(t)$ fixed at the trailing edge of the structure with $A(0) = (0.3\text{ m},\ 0,\ 0.05\text{ m})$, and $B(t)$ fixed at the middle position of the plate with $B(0) = (0.15\text{ m},\ 0,\ 0.05\text{ m})$, additional, six monitoring points of flow fields near trailing edge of the plate are labeled point 1, point 2, ⋯, point 6.

The geometry, the mesh and the boundary conditions are given in Fig. 3. There are solid walls at the top, at the bottom and at the two sides of the channel. Non-slip boundary conditions were applied at the solid walls. At the channel exit only pressure was prescribed ($P = 0$). At the channel entrance the velocity profile corresponds to a fully developed flow, perpendicular to the entrance plane. The flow Reynolds number Re is 25,500, the turbulent flow is modeled by standard $k - \varepsilon$ two equations model. To the best of according with the experimental boundary condition, the inlet velocity is set according to the measured data and approximately expressed as

$$u_{in} = V(1 + A\sin\omega t) \tag{35}$$

Where $A = 0.025$ is the measured velocity wake amplitude ration relative the average inflow velocity, $\omega = 0.75\pi$ is the nearly circular frequency measured of velocity fluctuation.

The computational region of fluid is divided two parts, one is the Euler region, another is ALE region. Total 170,000 tetrahedron meshes are used in the ALE region and 40,000 hexahedron meshes are used in the Euler region. The discretisation of the solid is composed of 1,200 eight-node hexahedron elements. The non-dimensional parameter $\alpha = \beta = \gamma = 0.5$ is adopted.

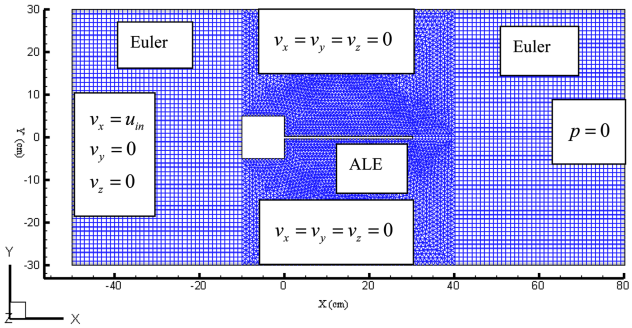

Fig. 3 Computational mesh and boundary conditions for fluid

5.1.2 Computational results

Fig. 4 show the evolvements of spanwise vorticity (ω_z) of some fluid monitoring points. Although these points in space are symmetry about the plate, the spanwise vorticity distribution doesn't keep symmetry, which is mainly ascribed to the shear layers developed on both sides of the vibrating plate, the shedding vortex upstream and the wake flow as well as the interaction among them. It is also seen that the periodicity of vortex structure downstream is broken due to the vortex induced vibration, while the pulsatile flow in inlet is periodic.

The evolvements of turbulent eddy frequency of some fluid monitoring points are shown in Fig. 5. The turbulent eddy frequency of these fluid monitoring points positioned the trailing edge of the

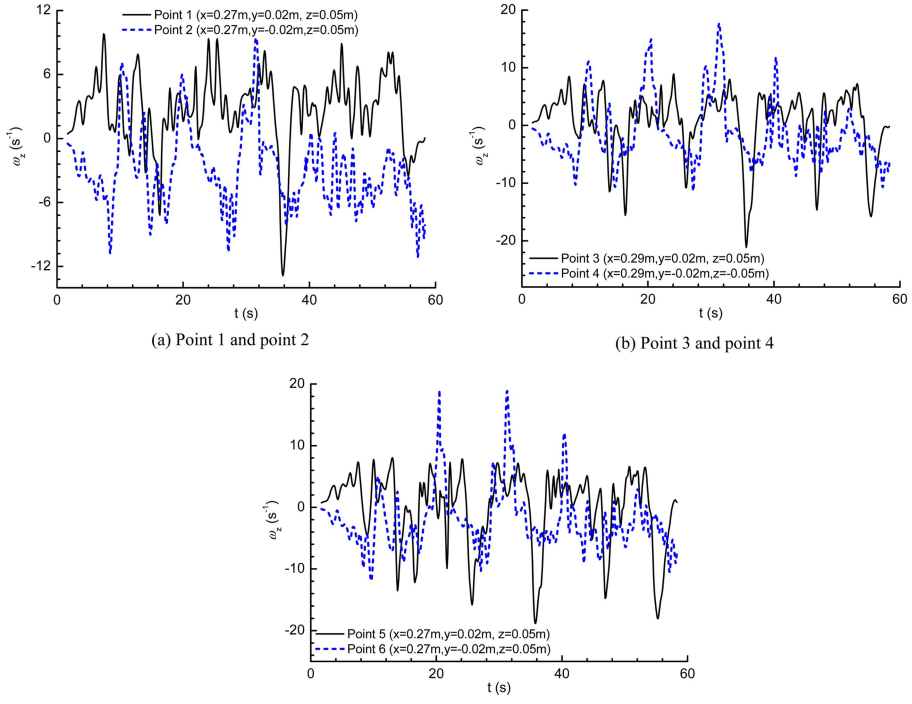

(a) Point 1 and point 2

(b) Point 3 and point 4

(c) Point 5 and point 6

Fig. 4 Evolvement of typical spanwise vorticity (ω_z) at different space

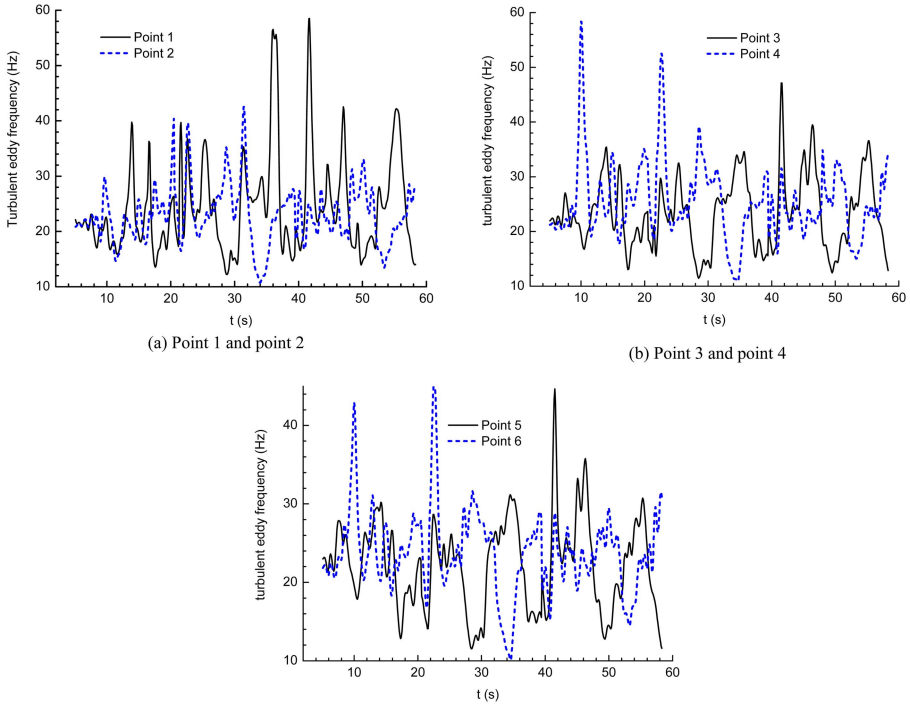

(a) Point 1 and point 2

(b) Point 3 and point 4

(c) Point 5 and point 6

Fig. 5 Evolvement of turbulent eddy frequency at different space

plate are all largely fluctuation from 10 Hz to 60 Hz, which cover the first and second natural frequency of the plate, may be induced the clap or resonance response of the structure (Further be seen in Fig. 6).

Fig. 6 shows the displacement evolvement of two monitoring points of structure. Some conclusions can be present as follows. Firstly, the vibration of plate is non-periodic and asymmetric. Secondly, the maximum vibrating amplitude is about 3 times higher than the averaged vibrating amplitude, it is can be concluded that the resonance may be occurrence when the eddy frequency of flow is closed to the natural frequency of structure. For example, the turbulent eddy frequency of point 4 is about 60 Hz at 10.2 s and 21.7 s, shown in Fig. 4(b), which is near to the second natural frequency of the structure, then the structure vibrating displacement amplitude is up to local peak at 12.9 s and 22.7 s, respectively. The turbulent eddy frequency of point 4 is about 10 Hz at 34.3 s, shown in Fig. 4(b), which is near to the first natural frequency of the structure, then the structure vibrating displacement amplitude is up to maximum at 34.6 s. Thirdly, the strong vibration of the plate has a significant influence on the flow, which causes that the turbulent eddy frequency rapidly shift and deviate the eigen-frequency of the structure. This is evident from phenomena such as lock-in - which is the synchronization of the plate motion and the vortex shedding over a certain range of free stream velocities around the resonance velocity, or beat - which happens at a free-stream velocity lower or higher than that of lock-in, in the stage of the build up of oscillation, for example, the vibrating displacement of the free end of structure is up to local peak at 12.9 s (lock-in occur), however, the displacement is illustrated rise-decrease-raise at 22.7 s (beat occur).

5.1.3 Comparison of numerical and experimental results

An accelerating sensor DH-201 is mounted on the position of point *B* for measuring the flow-induced vibrating displacement. Fig. 6 also shows the measured vibrating displacements of the mid of the plate against time and the comparison between the measuring and calculating vibrating displacement is listed in Table 1. It can be seen that the maximum of vibrational amplitude by numerical calculation are very close to that of the measure. The good agreement between the numerical and experimental data is achieved.

To validate our methodology and to assess the accuracy of the numerical results, we have performed extensive comparisons with available experimental results. The pressure sensors that are made by UAS Kulite, LL-072-25A, were mounted on the surface at the free end of the plate (Point *A*). The comparisons of the computation and the measured pressure at these points are shown in Fig. 7. it can be seen that a better agreement between our computations with FSI and the experimental data as a whole, while a little difference in predicting the maximum of pressure fluctuation, because there is more complex flow due to the effects of upstream shedding vortex and the development of shear layers along the plate surface as well as the deformation of plate, also, the inlet wake is not perfectly same between the numerical simulation and experiment. The first and second dominant frequencies of calculating fluctuating pressure are 0.137 Hz and 1.454 Hz, respectively, corresponding to that of measuring fluctuating pressure, are 0.131 Hz and 1.641 Hz, the results in this paper show that the simulations in which FSI is considered are close to the measure.

5.2 Blood flow through an idealised cerebral arterial aneurysm

This three-dimensional biomedical problem is motivated by the growing need for accurate bio-

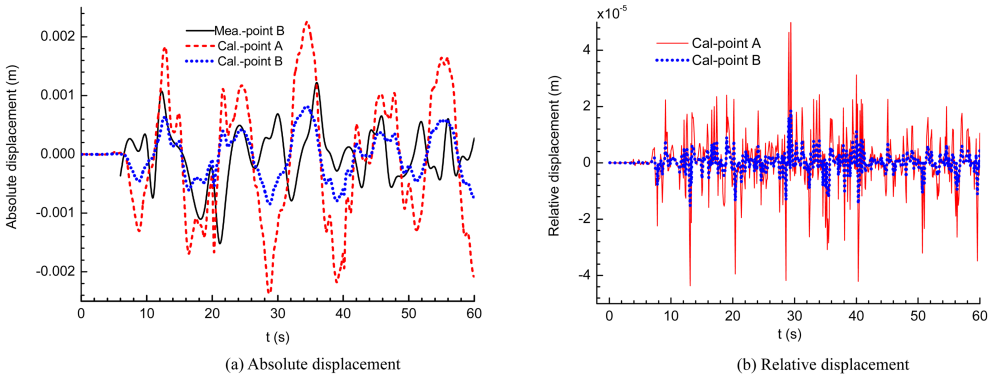

(a) Absolute displacement (b) Relative displacement

Fig. 6 Evolvement of displacement of structure at typical points

Table 1 Comparing of vibrating displacement of structure between the calculation and experiment

Point *B*	Average	Maximum (along positive *z* axis)	Maximum (along negative *z* axis)
Measure value (m)	10.89×10^{-5}	2.19×10^{-3}	2.24×10^{-3}
Calculation value (m)	9.92×10^{-5}	2.26×10^{-3}	2.37×10^{-3}
Error (%)	8.9%	3.1%	5.8%

medical modelling of the human body, specifically in the area of cardiovascular medicine. In this study, a three-dimensional cerebral arterial aneurysm modeling is simulated. The length and diameter of the blood vessel are taken as 10 mm and 1 mm, respectively, with a circular cross section. The idealized form of the aneurysm is introduced as a sphere of diameter 1 mm with centre offset by 0.75 mm from the vessel centreline. The thickness of the aneurysm wall, based upon information extracted from medical imaging of real patients, is taken as $t = 0.075$ mm. The discretisation of the three-dimensional fluid domain is composed of 193,595 tetrahedra (34,749 nodes), with the structure modelled using 2228 3-noded triangular elements (1140 nodes). The deformable membrane component is modelled in 3D using a linear elastic material. The flowrate waveform with the Womersley profile based on the measured velocity is shown in Fig. 8(a). According to Womersley formulation (Womersley 1955), the resulting pressure waveform is shown in Fig. 8(b). No-slip condition is applied at the arterial wall. In the structural mechanics computations, the hemodynamic

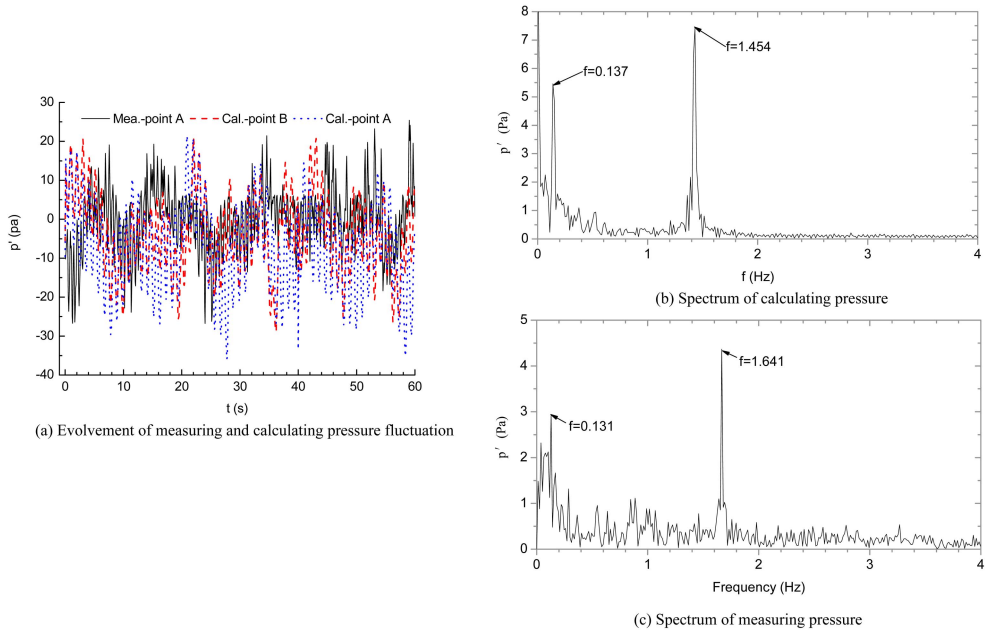

(a) Evolvement of measuring and calculating pressure fluctuation

(b) Spectrum of calculating pressure

(c) Spectrum of measuring pressure

Fig. 7 Comparing of the pressure between the calculation and experiment

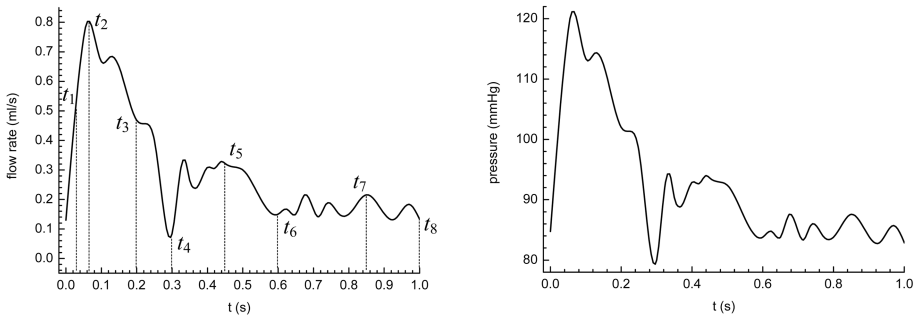

(a) Flowrate waveform

(b) Pressure waveform

Fig. 8 Transient behavior of the boundary conditions in a cardiac cycle

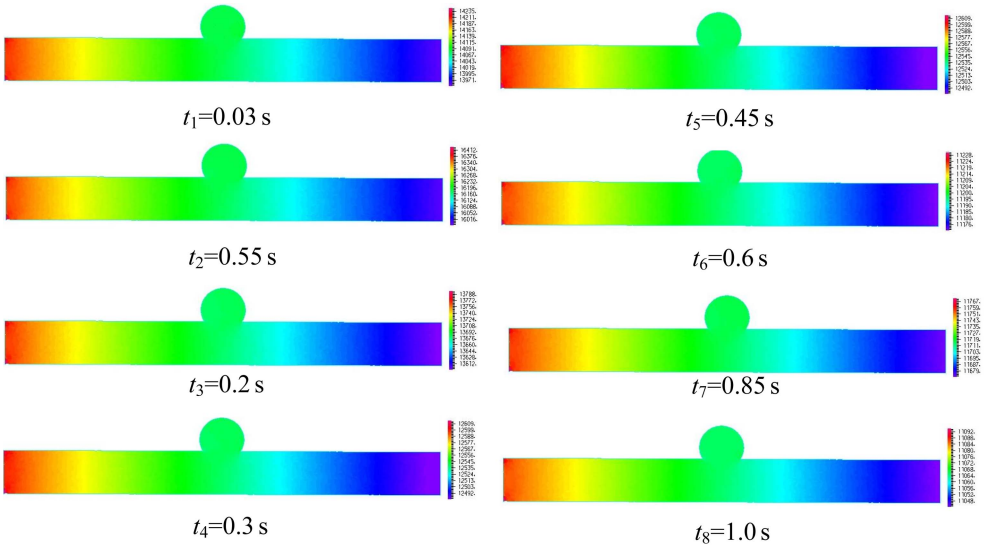

Fig. 9 Fluid pressure at different time

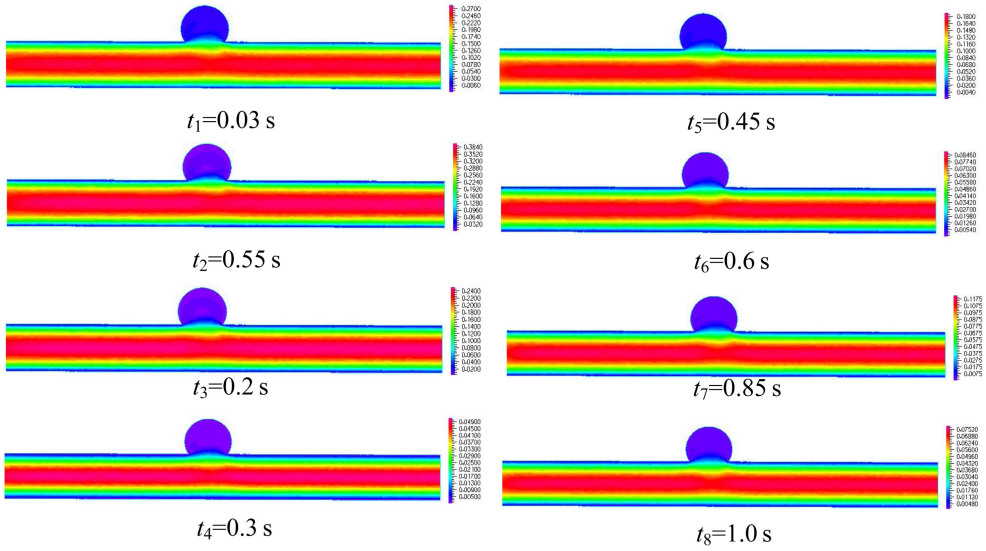

Fig. 10 Fluid velocity at different time

force at the interface between the blood and arterial wall is used as the surface force. The ends of the aneurysm are held fixed by specifying zero-displacement boundary conditions. The initial displacements and stresses are set to zero. The patient case is considered: Normal blood pressure, with a base (diastole) pressure of 80 mmHg and a peak (systole) pressure of 120 mmHg. The non-dimensional parameter $\alpha = \beta = \gamma = 0.5$ is adopted.

Cuts through the domain, shown in Figs. 9 and 10, reveal the fluid pressure and velocity profiles within the aneurysm. It can be observed that the fluid pressure and velocity does not change significantly in the area of the aneurysm. However, there is continuous fluid flow into the aneurysm

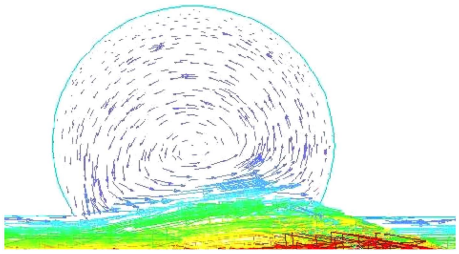

Fig. 11 Velocity vector indicating rotational flow within the aneurysm

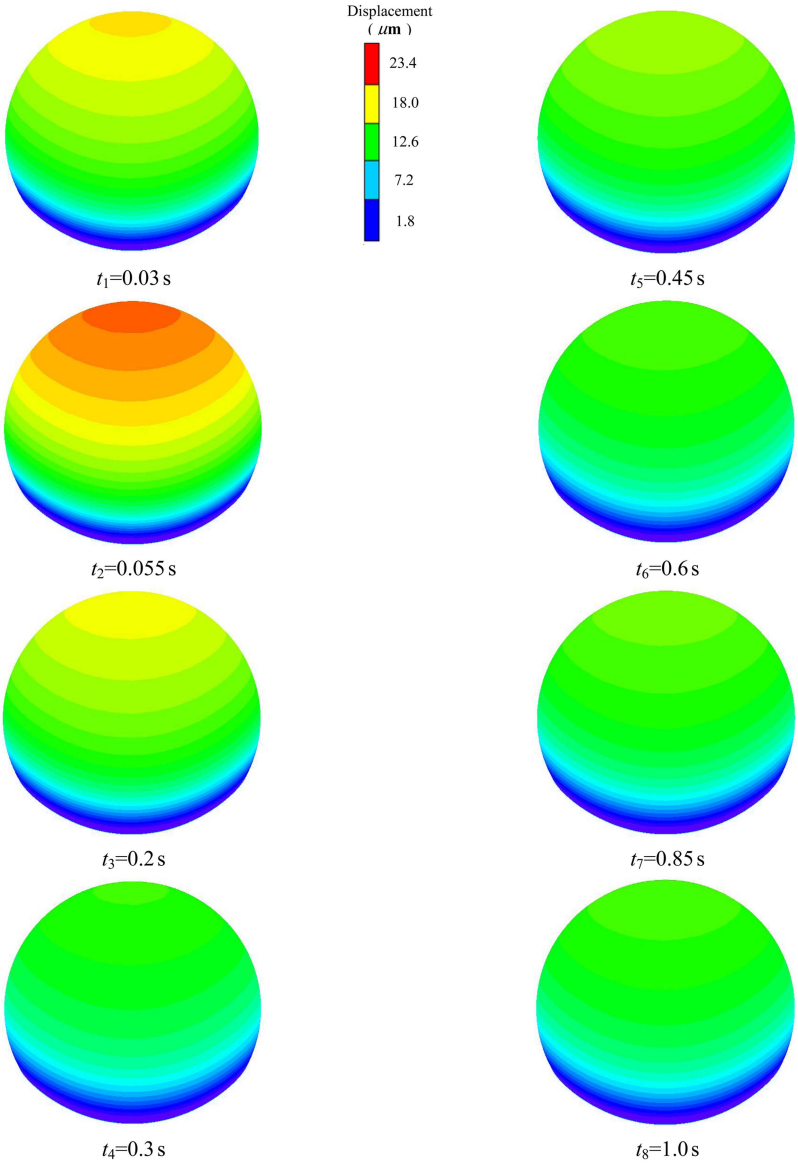

Fig. 12 Displacement over the aneurysm at different time

with an anticlockwise rotational flow within the aneurysm, evident in the plot of velocity vector in Fig. 11.

Fig. 12 shows the evolution of the aneurysm wall movement in time over the systolic/diastolic cycles. Analysis of these results shows that in the case of normal blood pressure, at peak flow the base flow causes the aneurysm to swell by 2.34×10^{-2} mm (2.4% of the radius). It is also seen that the aneurysm wall movement are largely different at different time.

6. Conclusions

A computational partitioned coupling strategy for the modeling of the interaction between pulsatile flow and large deformation structure has been presented, enabling a modular approach to be adopted for the fluid, structure and moving interface subproblems. The effectiveness of the algorithm is demonstrated with respect to experimental results for a benchmark example. Conservative transfer of information at the fluid-structure interface is combined with an effective predict-correct iterative scheme to enable implicit coupling of the interacting fields at each time increment. The three-dimensional unsteady incompressible fluid is solved using a powerful implicit time stepping technique and an ALE formulation for moving boundaries. A finite element dynamic analysis of the highly deformable structure is carried out with a numerical strategy combining the implicit Newmark time integration algorithm with a Newton-Raphson second-order optimisation method. This partitioned strategy seems ideally suited to the modelling of fluid-structure interaction problems even for pulsatile flow and very flexible structures and further work on a coupling strategy with improved efficiency is currently in preparation.

Acknowledgments

The authors thank the National Natural Science Foundation of China (NSFC) (No. 11002063, 11262008) for financial support for this research.

References

Bletzinger, K.U., Gallinger, T., Kupzok ,A. and Wuchner. R. (2006), "Partitioned strategies for optimization on FSI", *Proceedings of the European conference on computational fluid dynamics*, Delft.

Blom, F.J. (1998), "A monolothical fluid-structure interaction algorithm applied to the piston problem", *Comput. Method. Appl. M.*, **167**, 369-391.

Bungartz, H.J. and Schafer, M. (2006), (Eds.), *Fluid-structure interaction: modeling, simulation, optimization*, New York: Springer.

Donea, J. (1983), *Arbitrary Lagrangian-Eulerian finite element methods*, (Eds. Belytschko, T. and Hughes, T.J.R.) *Computational Methods for Transient Analysis*, Elsevier, Amsterdam.

Donea, J, Jiuliani, S. and Halleux, J.P. (1982), "An arbitrary Lagrangian-Eulerian finite element method for transient dynamic fluid-structure interaction", *Comput. Method. Appl. M.*, **33**(1-3), 689-723.

Farhat, C. and Lesoinne, M. (2000), "Two efficient staggered algorithms for the serial and parallel solution of three-dimensional nonlinear transient aeroelastic problems" *Comput. Method. Appl. M.*, **182**(3-4) 499-515.

Farhat, C., Pierson, K. and Degand, C. (2000), "CFD based simulation of the unsteady aeroelastic response of a maneuvering vehicle", *Proceedings of the 38th AIAA Aerospace Sciences Meeting and Exhibit*.

Farhat, C., van der Zee, K.G. and Geuzaine, P.H. (2006), "Provably second-order time-accurate loosely-coupled solution algorithms for transient nonlinear computational aeroelasticity", *Comput. Method. Appl. M.*, **195**(17-18), 1973-2001.

Ge, L. and Sotiropoulos, F. (2007), "A numerical method for solving the 3D unsteady incompressible Navier Stokes equations in curvililinear domains with complex immersed boundaries", *J. Comput. Phyis.*, **225**(2), 1782-1890.

Geuzaine, P., Grandmont, C. and Farhat, C. (2003), "Design and analysis of ALE schemes with provable second-order timeaccuracy for inviscid and viscous flow simulations", *J. Comput. Phys.*, **191**(1), 206-227.

Guruswamy, G.P. and Byun, C. (1994), "Direct coupling of Euler flow equations with plate finite element structures", *AIAA J.*, **33**(2), 375-377.

Heil, M. (2004), "An efficient solver for the fully coupled solution of large-displacement fluid-structure interaction problems", *Comput. Method. Appl. M.*, **193**(1-2), 1-23.

Hieber, S.E. and Koumoutsakos, P. (2008), "An immersed boundary method for smoothed particle hydrodynamics of selfpropelled swimmers", *J. Comput. Phys.*, **227**(19), 8636-8654.

Hübner, B., Walhorn, E. and Dinkler, D. (2004), "A monolithic approach to fluid-structure interaction using space-time finite elements", *Comput. Method. Appl. M.*, **193**(23-26), 2087-2104.

Hughes, T.J.R., Liu, W.K. and Zimmermann, T.K. (1981), "Lagrangian-Eulerian finite element formulation for incompressible viscous flows", *Comput. Method. Appl. M.*, **29**(3), 329-349.

Koobus, B. and Farhat, C. (1999), "Second-order time-accurate and geometrically conservative implicit schemes for flow computations on unstructured dynamic meshes", *Comput. Method. Appl. M.*, **170**(1-2), 103-129.

Lee, T.R., Chang, Y.S., Choi, J.B., Kim, D.W., Liu, W.K. and Y.J. Kim (2008), "Immersed finite element method for rigid body motions in the incompressible Navier-Stokes flow", *Comput. Method. Appl. M.*, **197**(35-38), 2305-2316.

Lesoinne, M., Farhat, C. and Maman, N. (1996), "Geometric conservation laws for problems involving moving boundaries and deforming meshes, and their impact on aeroelastic computations", *Comput. Method. Appl. M.,* **134**(1-2), 71-90.

Liew, K.M., Wang, W.Q., Zhang, L.X. and He, X.Q. (2007), "A computational approach for predicting hydro-elasticity of flexible structures based on the pressure poisson equation", *Int. J. Numer. Meth. Eng.*, **72**(13), 1560-1583.

Nkonga, B. and Guillard, H. (1994), "Godunov type method on non-structured meshes for three-dimensional moving boundary problems", *Comput. Method. Appl. M.*, **113**(1-2), 183-204.

Peskin, C.S. (1972), "Flow patterns around heart valves: a numerical method", *J. Comput. Phys.*, **10**(2), 252-271.

Ramaswamy, B. and Kawahara, M. (1987), "Arbitrary Lagrangian-Eulerian finite element method for unsteady, convective, incompressible viscous free surface fluid flow", *Int. J. Numer. Meth. Fl.*, **7**, 1053-1075.

Rugonyi, S. and Bathe, K.J. (2001), "On finite element analysis of fluid flows fully coupled with structural interactions", *Comput. Model. Eng. Sci.*, **2**(2), 195-212.

Sarrate, J., Huerta, A. and Donea, J. (2001), "Arbitrary Lagrangian-Eulerian formulation for fluid-rigid body interaction", *Comput. Method. Appl. M.*, **190**(24-25), 3171-3188.

Stein, K.R., Benney, R.J., Tezduyar, T.E., Leonard, J.W. and Accorsi, M.L. (2001), "Fluid-structure interactions of a round parachute: modeling and simulation techniques", *J. Aircraft*, **38**, 800-808.

Tezduyar, T.E., Sathe, S., Stein, K. and Aureli, L. (2006), *Modeling of fluid-structure interactions with the space-time techniques, Fluid-Structure Interaction* (Eds. Bungartz, H.J. and Schafer, M.), Lecture Notes on Computational Science and Engineering, Springer.

Thomas, P.D. and Lombard, C.K. (1979), "Geometric conservation law and its application to flow computations on moving grids", *AIAA J.*, **17**, 1030-1037.

Torii, R., Oshima, M., Kobayashi, T., Takagi, K. and Tezduyar, T.E. (2008), "Fluid-structure interaction modeling of a patientspecific cerebral aneurysm", *Comput. Mech.*, **43**(1), 151-159.

Venkatakrishnan, V. and Mavriplis, D.J. (1996), "Implicit method for the computation of unsteady flows on unstructured grids", *J. Comput. Phys.*, **127**(2), 380-397.

Wang, W.Q., He, X.Q., Zhang, L.X, Liew, K.M. and Guo, Y.K. (2009), "Strongly coupled simulation of fluid-structure interaction in a Francis hydroturbine", *Int. J. Numer. Meth.Fl.*, **60**(5), 515-538.

Womersley, J.R. (1955), "Method for the calculation of velocity, rate of flow and viscous drag in arteries when

the pressure gradient is known", *Physiology*, **127**, 553-563.
Zhang, L.X., Guo, Y.K. and Wang, W.Q. (2007), "Large eddy simulation of turbulent flow in a true 3D Francis hydro turbine passage with dynamical fluid-structure interaction", *Int. J. Numer. Meth. Fl*., **54**(5), 517-541.
Zhang, N. and Zheng, Z.C. (2007), "An improved direct-forcing immersed-boundary method for finite difference applications", *J. Comput. Phyis*., **221**(1), 250-268.
Roe, P.L. (1983), "Some contributions to the modeling of discontinuous flows", *Proceedings of the AMS/SIAM Seminar*, San Diego, USA.